

Lithium hexamethyldisilazide as electrolyte additive for efficient cycling of high-voltage non-aqueous lithium metal batteries

Received: 30 March 2022

Accepted: 4 November 2022

Published online: 15 November 2022

Check for updates

Danfeng Zhang^{1,2,6}, Ming Liu^{1,6}, Jiabin Ma^{1,2}, Ke Yang^{1,2}, Zhen Chen¹, Kaikai Li³, Chen Zhang¹, Yinping Wei^{1,2}, Min Zhou⁴, Peng Wang¹, Yuanbiao He¹, Wei Lv¹, Quan-Hong Yang⁵, Feiyu Kang^{1,2} & Yan-Bing He¹✉

High-voltage lithium metal batteries suffer from poor cycling stability caused by the detrimental effect on the cathode of the water moisture present in the non-aqueous liquid electrolyte solution, especially at high operating temperatures (e.g., ≥ 60 °C). To circumvent this issue, here we report lithium hexamethyldisilazide (LiHMDS) as an electrolyte additive. We demonstrate that the addition of a 0.6 wt% of LiHMDS in a typical fluorine-containing carbonate-based non-aqueous electrolyte solution enables a stable Li||LiNi_{0.8}Co_{0.1}Mn_{0.1}O₂ (NCM811) coin cell operation up to 1000 or 500 cycles applying a high cut-off cell voltage of 4.5 V in the 25 °C–60 °C temperature range. The LiHMDS acts as a scavenger for hydrofluoric acid and water and facilitates the formation of an (electro)chemical robust cathode|electrolyte interphase (CEI). The LiHMDS-derived CEI prevents the Ni dissolution of NCM811, mitigates the irreversible phase transformation from layered structure to rock-salt phase and suppresses the side reactions with the electrolyte solution.

Nickel-rich cathode such as LiNi_{0.8}Co_{0.1}Mn_{0.1}O₂ (NCM811) show significant promises to help lithium-ion batteries to achieve high specific energy (>400 W h kg⁻¹)^{1–4}, while many serious issues still remain including severe side reactions with conventional fluorine-containing carbonate-based liquid electrolyte solutions^{5–8}, rapid structural degradation^{9,10}, thermodynamic instability¹¹ and capacity decay¹² during cycling under high cut-off voltage (i.e., ≥ 4.5 V vs Li/Li⁺) and high operation temperature (i.e., ≥ 60 °C). The Ni⁴⁺ ions of delithiated NCM811 cathode are easily reduced to Ni²⁺ and Ni³⁺ ions by oxidation reaction of electrolyte, which leads to gas generation and impedance increase of the batteries⁹. Cation mixing of Ni²⁺ and Li⁺ also occurs to form rock-salt phase owing to their similar ionic radius, which leads to structure degradation and huge capacity loss, especially at 60 °C^{10–13}. It is generally considered that

the trace amount of H₂O in the electrolyte reacts with PF₆⁻ of the lithium hexafluorophosphate (LiPF₆) to generate corrosive hydrofluoric acid (HF)^{14–16}, which causes transition metal (TM) ions dissolution¹⁷, oxygen evolution from cathode surface, aluminum collector corrosion and irreversible cathode-electrolyte interphase (CEI) damage upon cycling and storage^{11,18}. The decomposition of the LiPF₆ salt exhibits strong correlation with the battery operation temperature and the thermal aggravation strongly promotes the salt decompositions¹⁹. In addition, the instable CEI at high cut-off voltage and high temperature causes excessive electrolyte oxidation and interface deterioration. Addressing these crucial issues is of great significance to pursue an effective strategy to achieve high-performance Li||NCM811 batteries at a wide operation temperature and high cut-off voltage.

¹Shenzhen All-Solid-State Lithium Battery Electrolyte Engineering Research Center, Institute of Materials Research (IMR), Tsinghua Shenzhen International Graduate School, Tsinghua University, Shenzhen 518055, China. ²School of Materials Science and Engineering, Tsinghua University, Beijing 100084, China. ³School of Materials Science and Engineering, Harbin Institute of Technology, Shenzhen 518055, China. ⁴School of Pharmacy, East China University of Science and Technology, Shanghai 200237, China. ⁵Nanoyang Group, State Key Laboratory of Chemical Engineering, School of Chemical Engineering and Technology, Tianjin University, Tianjin 300072, China. ⁶These authors contributed equally: Danfeng Zhang, Ming Liu.

✉ e-mail: he.yanbing@sz.tsinghua.edu.cn

Many efforts including doping, surface coating and electrolyte additives have been made to improve the structural and interfacial stability of NCM811 particles. For instance, doping of Ca^{2+19} , Al^{3+17} , Zr^{4+20} , and Nb^{5+21} can improve the structure stability of NCM811 by enlarging the Li slab distance. Constructing surface coating layers such as $\text{Al}_2\text{O}_3^{22}$, $\text{ZrO}_2^{23,24}$, and $\text{V}_2\text{O}_5^{25}$ on NCM811 particles can suppress the decomposition of electrolyte at early cycling stage to prevent the formation of metal fluorides and dissolution of TM ions induced by HF. However, the metal oxide coating layers easily react with HF, especially at high cut-off voltage and high temperature. Employing electrolyte additives to stabilize the CEI is an expeditious and convenient method to improve the performance of nickel-rich NCM by scavenging the H_2O , HF and PF_5 species²⁶. For instance, 4-fluorophenyl isocyanate²⁷, dimethoxydimethylsilane (DODSi)²⁸, and 3-(trimethylsilyl)-2-oxazolidinone (TMS-ON)¹⁷ could react with HF to suppress the interfacial reactions of cathode and electrolyte. The aluminum isopropoxide (AIP) could initiate in situ polymerization of ethylene carbonate (EC) to construct a polycarbonate-rich CEI on NCM811²⁹. However, the operation temperature of nickel-rich NCM batteries using above additives is limited to 45 °C owing to the reactivity of nickel-rich NCM cathode with liquid electrolyte, which causes the battery overcharge at higher temperature³⁰. In addition, the CEI built by additives isn't (electro)chemical robust and stable sufficiently to inhibit the catalytic side reactions between NCM811 cathode and electrolyte³¹. In practical operating conditions, the battery is heated due to the continuous heat generation³². Therefore, promoting the thermal stability of NCM811 batteries at higher than 45 °C is in urgent need for practical application. In addition, the onset oxidation potential of these additives on high nickel cathode is larger than 4 V, which is higher than the initial delithiated potential of NCM811 cathode (3.62 V)²⁸. The late formed CEI cannot timely suppresses the side reactions of cathode and non-aqueous electrolyte. Therefore, it is quite significant and critical to develop low oxidation potential electrolyte additives with integrated functions to simultaneously scavenge HF and preferentially construct CEI on NCM811 for advanced Li||NCM811 batteries under high voltage and elevated operation temperature.

Herein, we present a new multi-functional additive, lithium hexamethyldisilazide (LiHMDS) with a low oxidation potential, for NCM811, which improve the cycling stability of Li||NCM811 batteries at high-stress conditions such as high voltage (4.5 V) and high temperature (60 °C). The LiHMDS as a strong organic base with low onset oxidation potential not only scavenges HF and H_2O in electrolyte, but also preferentially creates a thin and robust CEI on NCM811 before oxidation of electrolyte, which effectively suppresses the irreversible structure transformation of NCM811 particles from layered structure to rock-salt phase, the dissolution of transition metal elements, and side reactions with electrolyte during long cycles. As a result, the Li||NCM811 coin cells with only 0.6 wt% LiHMDS in 1 M LiPF_6 carbonate-based electrolyte solution can stably cycle for 1000 times at 25 °C and 500 times at 60 °C under high cut-off voltage of 4.5 V, also using 50 μm thick Li metal negative electrodes and high mass-loading positive electrodes (i.e., 10 mg cm^{-2}) at 60 °C.

Results

Electrochemical performance of Li||NCM811 cells with LiHMDS

The cycling performance of the Li||NCM811 cells between 2.8 and 4.3 V at 25 °C is improved by LiHMDS as shown in Fig. 1a and Supplementary Fig. 1. The Li||NCM811 cell with 0.6 wt% LiHMDS (0.6 wt% LiHMDS was applied in the following cells with LiHMDS) presents the highest capacity retention of 71.24% after 1000 cycles at 90 mA g^{-1} , which is higher than that of Li||NCM811 cells (only using baseline electrolyte (BE) without LiHMDS) (27.12%). The coin cell was disassembled and noticed that a large area of cycled NCM811 cathode of BE cells spalled from the collector after ~400 cycles (Supplementary Fig. 2a). In addition, it is also possible to notice TMs dissolution, which transferred to

lithium metal anode (LMA) (Supplementary Fig. 2b). In sharp contrast, the cycled NCM811 cathode from LiHMDS cells presents intact structure after 400 cycles and the dissolution of transition metals seems to be hindered. Therefore, we speculate that the spalling of NCM811 cathode from the collector and dissolution of transition metals result in rapid capacity decline of BE cells after 400 cycles (Supplementary Fig. 2c and d). The cyclic voltammetry (CV) curves show that the Li||NCM811 cells with LiHMDS present better reversibility than the Li||NCM811 cells during 5 cycles from 3 to 4.5 V at both 25 and 60 °C (Supplementary Fig. 3). Accordingly, the Li||NCM811 cells with LiHMDS show higher capacity retention of 73.92% than Li||NCM811 cells (49.13%) after 1000 cycles between 3 and 4.5 V at 90 mA g^{-1} and 25 °C (Fig. 1b). In addition, the Li||NCM811 cells with LiHMDS exhibit better rate performance than the Li||NCM811 cells at 25 ± 1 °C (Fig. 1c). More significantly, the Li||NCM811 cells with LiHMDS show a cycling life of 500 times at 60 °C with average coulombic efficiency of 99.11% and capacity retention of 66.02% (Fig. 1d). The cycling performances of Li||NCM811 cells with LiHMDS are well positioned in the literature when compared to other research works that investigate non-aqueous electrolyte solution additives in lab-scale Li||NCM811 cells (Supplementary Table 1). In sharp contrast, the Li||NCM811 cells with BE display lower average coulombic efficiency of 93.48% and present micro short circuit after 200 cycles. Moreover, the Li||NCM811 cells with LiHMDS exhibit a smaller polarization than that of the Li||NCM811 cells (Supplementary Fig. 4). The average discharge voltage of the Li||NCM811 cells with BE drops from 3.84 to 3.66 V after 300 cycles at 60 °C, while that of the Li||NCM811 cells with LiHMDS retains quite stable value up to 3.79 V (Supplementary Fig. 5). Furthermore, the discharge capacity of the Li||NCM811 cells with LiHMDS reaches 180.7 and 163.8 mA h g^{-1} at the rate of 900 mA g^{-1} and 1800 mA g^{-1} under 60 °C, respectively, which is much higher than that of Li||NCM811 cells with BE (167.5 and 139.4 mA h g^{-1}) (Supplementary Fig. 6). Meanwhile, the LiHMDS enables 88.47% capacity retention of the Li||NCM811 cells with high NCM811 mass-loading of 10 mg cm^{-2} and thin lithium foil anode of 50 μm at the rate of 60 mA g^{-1} after 100 cycles under 60 °C, whereas the Li||NCM811 cells with BE present only 18.67% capacity retention for the same cycling conditions (Fig. 1e). This is due to that the side reactions between NCM811 and LMA with BE are more likely to occur than that with LiHMDS at elevated temperature and high cut-off voltage (Supplementary Figs. 7, 8), especially at the high cathode loading, which leads to larger consumption of LMA with only 50 μm thickness³³. When the LiHMDS-containing electrolyte is tested in pouch cell configuration, the capacity retention of pouch cell is 93.4% after 75 cycles at 36 mA g^{-1} under 60 °C (Supplementary Fig. 9), confirming that the LiHMDS can hinder the side reactions between NCM811 and LMA with BE. Such cycling and rate improvements of Li||NCM811 cell with LiHMDS at high voltage and high temperature demonstrate the compatibility of LiHMDS with both NCM811 cathode and LMA. A stable interphase at the NCM811 | liquid electrolyte interface may be constructed by LiHMDS, which suppresses the phase transition on the NCM811 particle and side reactions of NCM811 with electrolyte.

In order to simulate possible localized overheated battery, alternative testing at low (i.e., 25 °C) and high (i.e., 60 °C) temperatures was carried out (Fig. 1f). After 50 cycles at different temperatures, the Li||NCM811 cells with LiHMDS show higher capacity retention of 95.54% and 95.82% at 25 °C and 60 °C than the Li||NCM811 cells with BE (88.08% and 93.81%, respectively). The electrochemical impedance spectroscopy (EIS) measurements show that the charge transfer resistance (R_{ct}) of Li||NCM811 cells with BE increases from 10.74 Ω to 65.23 Ω after 100 cycles, while that of the Li||NCM811 cells with LiHMDS only increases from 5.11 Ω to 5.37 Ω after 100 cycles, supporting the speculation of the ability of LiHMDS to hinder the side reactions of NCM811 with electrolyte (Supplementary Fig. 10, Supplementary Table 2). In addition, we also assembled the graphite || NCM811 coin

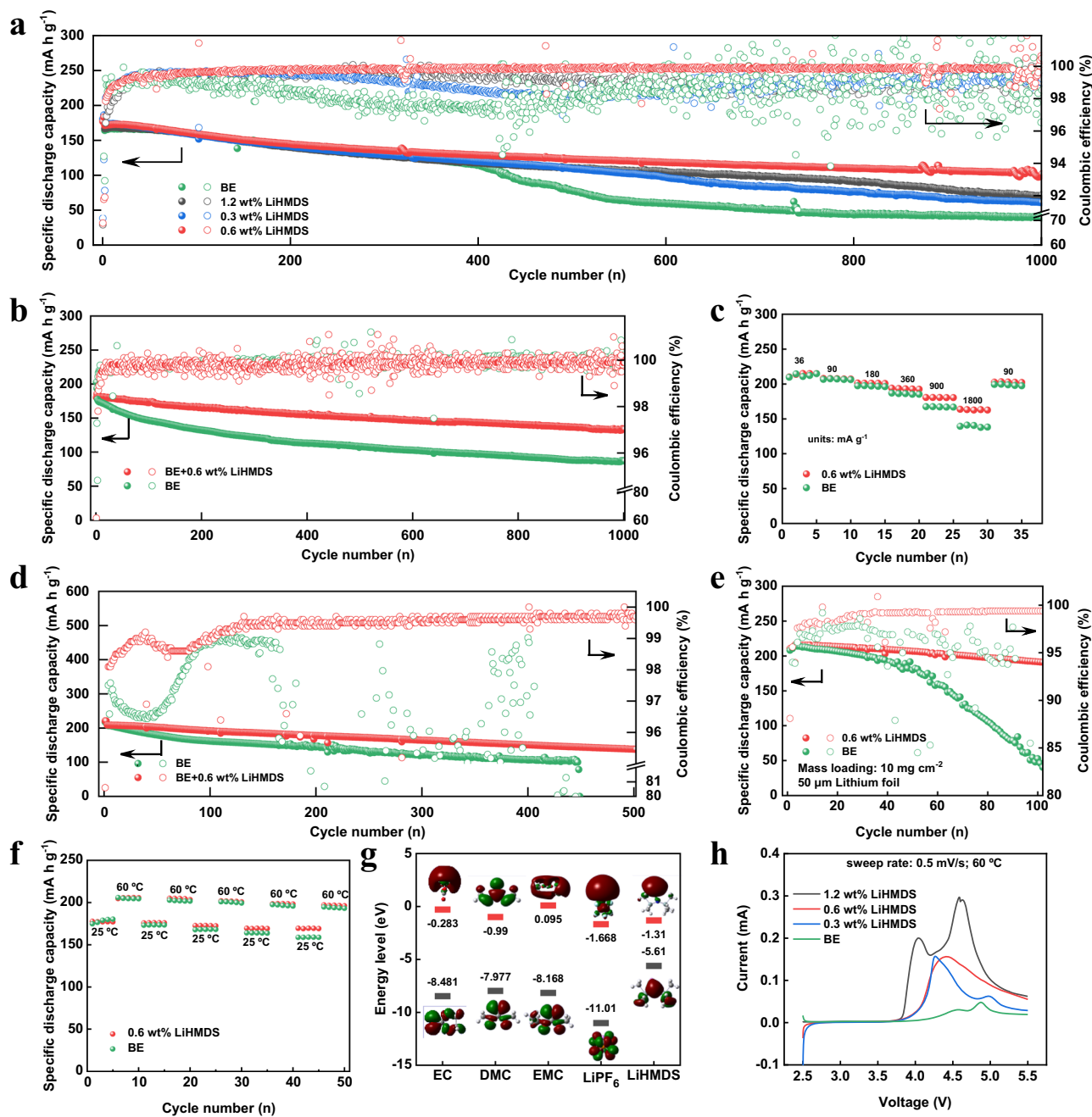


Fig. 1 | Electrochemical performance of Li||NCM811 cells with and without LiHMDS. **a** Cycling performance of Li||NCM811 cells with different amount of LiHMDS at 25 °C between 2.8 and 4.3 V, specific current is 180 mA g⁻¹. **b** Cycling performance at 25 °C between 3 and 4.5 V, specific current is 90 mA g⁻¹. **c** Rating performance at 25 °C. **d** Cycling performance at 60 °C between 3 and 4.5 V, specific current is 180 mA g⁻¹. **e** Cycling performance of thin Li

electrode || high loading NCM811 cells at 60 °C between 3 and 4.5 V, specific current is 60 mA g⁻¹. **f** Cycling performance under different temperature between 3 and 4.5 V, specific current is 60 mA g⁻¹. **g** HOMO and LUMO energy levels of EC, DMC, EMC, LiPF₆ and LiHMDS. **h** linear sweep voltammetry measurements of BE and BE with different amount of LiHMDS additives at 60 °C under sweep rate of 0.5 mV s⁻¹.

cells with LiHMDS, which present the capacity retention of 62.08% at 180 mA g⁻¹ after 200 cycles under 60 °C, which is higher than that of graphite || NCM811 cells with BE (50.62%) (Supplementary Fig. 11). Furthermore, the Li||LiNi_{0.5}Mn_{1.5}O₂ (LNMO) coin cells with LiHMDS also present better cycling performance at 147 mA g⁻¹ than the Li||LNMO cells with BE (Supplementary Fig. 12).

Effect of LiHMDS on the CEI of NCM811 cathode

The density functional theory (DFT) calculations present that the highest occupied molecular orbital (HOMO) level of the LiHMDS is -5.61 eV, which is higher than the other components of the electrolyte

(Fig. 1g). The linear sweep voltammetry (LSV) curves also show that the LiHMDS is oxidized from 3.8 V to form CEI (Fig. 1h)³⁴. These results indicate that the LiHMDS would be oxidized preferentially than electrolyte to form a new CEI on NCM811 cathode. The Si 2p spectra obtained from the ex situ X-ray photoelectron spectroscopy (XPS) measurements carried out on positive electrode sampled from cycled Li||NCM811 cells with LiHMDS show two peaks of Si-N (103.7 eV) and Si-C peak (101.8 eV) on the depth profiling compared to the XPS measurements carried out on positive electrode sampled from cycled Li||NCM811 cells with BE (Fig. 2a, b), suggesting the deposition of oxidation products of LiHMDS on NCM811 surface. The signals of Si-N

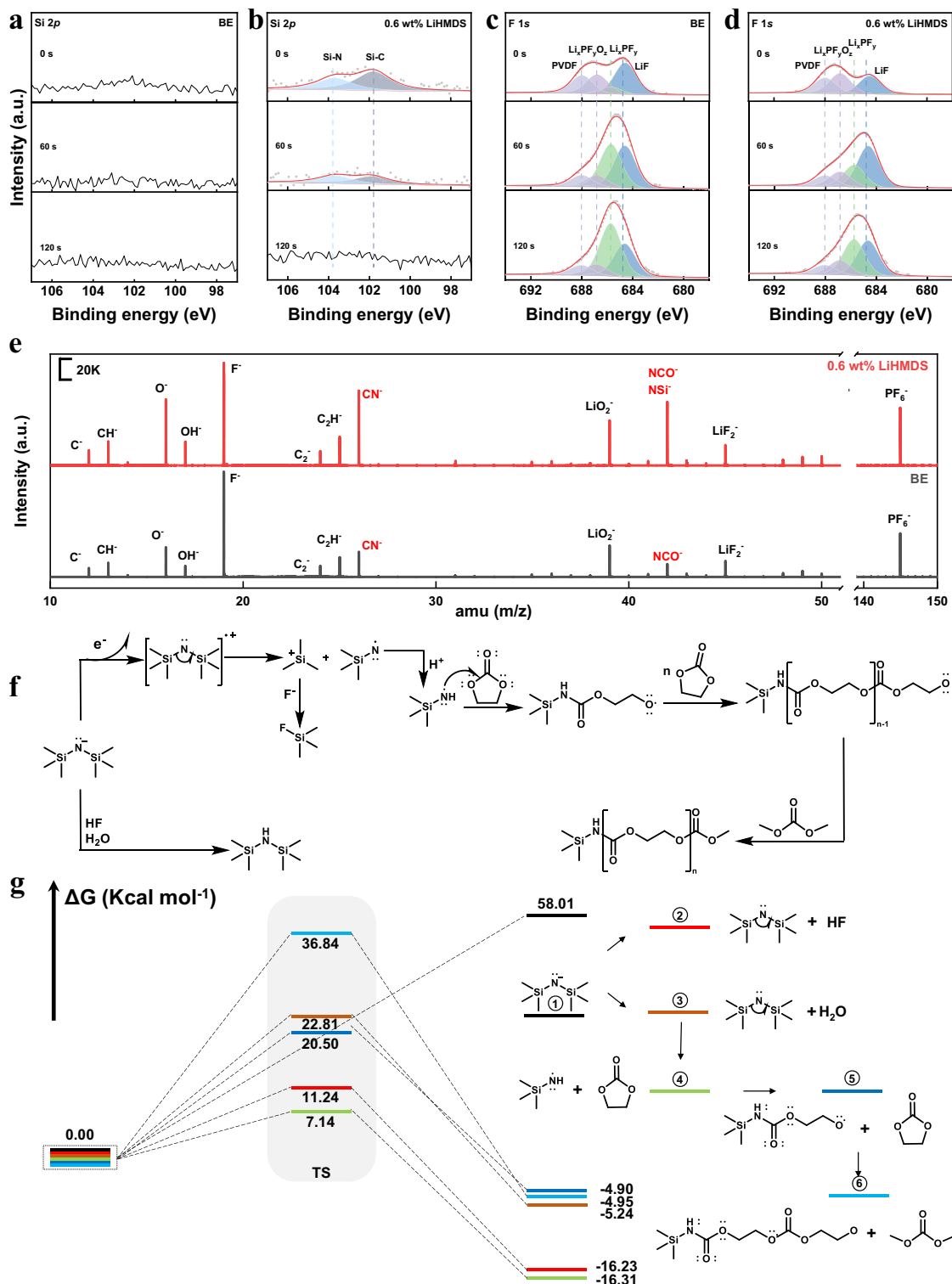


Fig. 2 | Surface component analysis of NCM811 cathode. Ex situ XPS measurements and analysis of NCM811 cathode retrieved from **a, c** Li||NCM811 cells and **b, d** Li||NCM811 cells with LiHMDS after 100 cycles at 60 °C, the charging/discharging current were 180 mA g⁻¹/180 mA g⁻¹. **a, b** Si 2p. **c, d** F 1s. **e** Ex situ TOF-SIMS

analysis of NCM811 cathode retrieved from Li||NCM811 cells after 5 cycles at 60 °C, the charging/discharging current were 18 mA g⁻¹/18 mA g⁻¹. The cell was disassembled at fully discharged state. **f** Possible reaction mechanisms of LiHMDS. **g** Reaction energy diagram of LiHMDS.

peak and Si-C peak only appear on the cathode surface suggest that the continuous decomposition of electrolyte solvent on the NCM811 cathode surface is inhibited once a thin and robust CEI layer is formed owing to the oxidation of LiHMDS. Compare to N 1s XPS spectra obtained from the ex situ measurements of positive electrode sampled

from cycled Li||NCM811 cells with BE, the samples with LiHMDS show a N-Si peak (398.3 eV), which confirms that the LiHMDS participated in CEI formation (Supplementary Fig. 13a, b). In addition, the P 2p spectra of Li||NCM811 cell with LiHMDS show a presence of Li_xPO_yF_z (Supplementary Fig. 13c, d), which can scavenge the dissolved TMs (such as

Co²⁺ and Ni²⁺) in the electrolyte to inhibit the TMs transfer to the LMA³⁵. The lower intensity of Li_xPF_y (686.8 eV) appeared in the F 1s spectra for the NCM811-based positive electrodes sampled from the cycled Li||NCM811 cells with LiHMDS indicates that the LiHMDS could suppress the decomposition of LiPF₆^{32,36,37} (Fig. 2c, d). Furthermore, for Li 1s and F 1s XPS spectra, the LiF content in CEI using LiHMDS is higher than BE after Ar⁺ etching for 60 s and 120 s, which can enhance the strength of the CEI (Fig. 2c, d, Supplementary Fig. 13e, f). Therefore, the LiHMDS promotes the formation of more inorganic species such as LiF and Li_xPO_yF_z in the CEI (Supplementary Fig. 14). The O 1s spectra of the cycled NCM811 cathode sampled from Li||NCM811 cells with BE electrolyte show a peak at 530 eV³⁸ (Supplementary Fig. 15a), which is ascribed to the metal oxide bonds (M-O) of NCM811, indicating that the uneven CEI formed on NCM811 particles using BE is unable to effectively passivate the highly active cathode surface (Supplementary Fig. 7b, c). In contrast, a weak M-O peak for the O 1s spectra and weak signals (Ni²⁺, Ni³⁺) for the Ni 2p spectra on the surface of NCM811 cathode sampled from Li||NCM811 cells with LiHMDS before etching appear (Supplementary Fig. 15b–d), indicating that a uniform CEI was formed on NCM811 surface. The O 1s spectra of the NCM811 cathode sampled from Li||NCM811 cell with LiHMDS on the depth profiling after etching for 120 s is similar to that of the pristine NCM811 particle, which indicates that LiHMDS is preferentially oxidized before electrolyte solvents (Supplementary Fig. 16).

Ex situ time-of-flight secondary ion mass spectrometry (TOF-SIMS) measurements were carried out on cycled positive electrodes to further identify the CEI components (Fig. 2e). The species with CN⁻ and NCO⁻ (NSi⁻) appear at $m/z = 26$ and $m/z = 42$, respectively, and their intensities for Li||NCM811 cell with LiHMDS are higher than those of Li||NCM811 cell with BE, confirming that the LiHMDS was oxidized on the surface of NCM811 cathode. We illustrate the possible two-stage reaction mechanisms of LiHMDS in Fig. 2f. First, the LiHMDS can be preferentially oxidized to form the radical anions, and then the radical anions capture the protons produced by the decomposition of carbonate solvents during cycling process and form the final radicals, which would polymerize with the EC and terminated by dimethyl carbonate (DMC) or ethyl methyl carbonate (EMC), thus forming a thin and uniform CEI film on the cathode surface³⁹. Second, the LiHMDS can capture HF and trace amount of H₂O in the electrolyte to form HMDS and other inorganic products (LiF and LiOH). We calculated the reaction energies (ΔG) of LiHMDS with HF and H₂O by DFT method. The energies of LiHMDS reacted with HF and H₂O are -16.23 and -5.24 kcal mol⁻¹, respectively. These results suggest that the LiHMDS can react spontaneously with HF and H₂O. In addition, the intermediates also can continue to spontaneously react with HF and H₂O, forming radicals to initiate the ring-opening polymerization reaction of EC (Fig. 2g).

Effect of LiHMDS on the structural evolution of NCM811

Operando X-ray diffraction (XRD) measurements were carried out to investigate the structural evolution of NCM811 cathode with different electrolytes during charge-discharge process (Fig. 3a, b). The (003) and (101) peaks intensity and the Bragg angle of NCM811 cathode cycled in BE change markedly during the phase transition from H1 phase to M phase at -3.8 V (Supplementary Fig. 17). After transition to the H2 phase, the (003) peak starts to shift left and then right, which corresponds to a phase transition from H2 to H3 phase with a reduced interlayer spacing⁴⁰. Left/right (003) peak shifts related to lattice expansion/contraction. Noticeably, the change of the (003) peak position of cycled NCM811 cathode using LiHMDS is much less than that using BE, which means that the change of lattice parameter c is hindered by LiHMDS during the charge process⁴⁰. In addition, the (101) peak using LiHMDS related to the lattice parameter a shifts less during the whole charge process. These results confirm that the cycled NCM811 cathode with LiHMDS presents a more reversible structural

evolution, which maintains well during cycle. Moreover, the XRD patterns show that the separation of (006)/(102) and (108)/(110) peaks is more clear for the cycled NCM811 with LiHMDS (Fig. 3c–e), indicating that the structure transformation from layered to rock salt phase is successfully suppressed⁴¹. The lower intensity ratio of R-factor (I(006)+I(012))/I(101) also suggests the good structure stability of cycled NCM811 with LiHMDS (Supplementary Fig. 18)⁴².

The improved structural stability of NCM811 during cycling with LiHMDS is attributed to the optimized CEI formed by LiHMDS. Ex situ TEM measurements of cycled positive electrodes show that a uniform and amorphous CEI with thickness of 5 nm was formed on the surface of NCM811 using LiHMDS after 100 cycles at 60 °C (Supplementary Figure 7a), much more uniform than that formed using BE (3 nm – 20 nm) (Supplementary Fig. 7b, c). The formation of the nanometric and uniform CEI indicates that the unwanted species like HF in the electrolyte have been sequestered completely by the LiHMDS, and thus no damage on the CEI occurs. Consequently, the NCM811 particles are protected by the CEI from possible side reaction with the electrolyte, which can avoid the reduction of the high valence Ni⁴⁺ in the delithiated NCM811 and suppress the phase transition from layered structure to rock-salt phase (Fig. 3f). Ex situ TEM measurements of cycled positive electrodes show that the layered structure is well preserved from the surface to the bulk after cycling with LiHMDS and negligible rock-salt phase formation was formed. On the contrary, a thicker rock-salt phase is observed on the surface region of the NCM811 particle cycled in BE (Fig. 3g)⁴⁰.

We also conducted an accelerated degradation test by holding the fully charged Li||NCM811 cells at 4.5 V (Supplementary Fig. 19). The Li||NCM811 cells with LiHMDS present a quasi-steady-state leakage current of -5 μ A after 2 h hold, while the leakage current of cell using BE slowly decreases and reaches a minimum value of 15 μ A after 12 h hold. The larger 4.5 V float-test leakage current suggests that more side reactions occur for the cell cycled with BE than that with LiHMDS. This result further proves that a diminished side reactions rate and passivated NCM811 cathode surface using LiHMDS are achieved due to formation of a thin and robust CEI⁴². Furthermore, the ex situ scanning electron microscopy (SEM) micrographs of cycled positive electrodes show intergranular macro cracking on the NCM811 particle with BE, while the cycled NCM811 cathode with LiHMDS did not experience intergranular cracking and maintain the structure (Supplementary Figs. 20 and 21). The intergranular macro cracking were generated owing to the internal strain inside the particles induced by volume change during the charge-discharge process⁴³. As a result, more fresh interfacial areas are exposed to electrolyte, resulting in rapid capacity fade and formation of thick CEI on NCM811 particle with BE.

Effect of LiHMDS on the solid electrolyte interphase (SEI) of LMA

The LiHMDS is also beneficial for the formation a stable SEI and improve the Li stripping/plating process on the LMA. Via ex situ measurements, the P 2p and Ni 2p XPS spectra of LMA cycled with LiHMDS and BE show different components. A relatively high fraction of Li_xPF_y, Li_xPO_yF_z, NiF₂ and Ni metal were observed on the cycled LMA surface with BE (Supplementary Fig. 22a–c). The formation of Li_xPF_y and Li_xPO_yF_z were attributed to the decomposition of LiPF₆ salt, and NiF₂ was formed due to the HF induced dissolution of Ni in NCM811. The Ni metal in the SEI layer results from the reduction of dissolved Ni²⁺ by lithium metal. The TM elements on the LMA surface leads to the SEI damaging⁴⁴, consumption of electrically active Li and increase of cell impedance⁴⁴. In sharp contrast, a smaller amount of Li_xPF_y, Li_xPO_yF_z, NiF₂ and Ni element were found on the cycled LMA with LiHMDS (Supplementary Fig. 22d, e), indicating that the LiHMDS inhibits the lithium salt decomposition and suppresses the dissolution of TM ions¹⁷. In addition, there is only LiF examined in the cell with LiHMDS (Supplementary Fig. 22f) compared to the LMA cycled in the BE

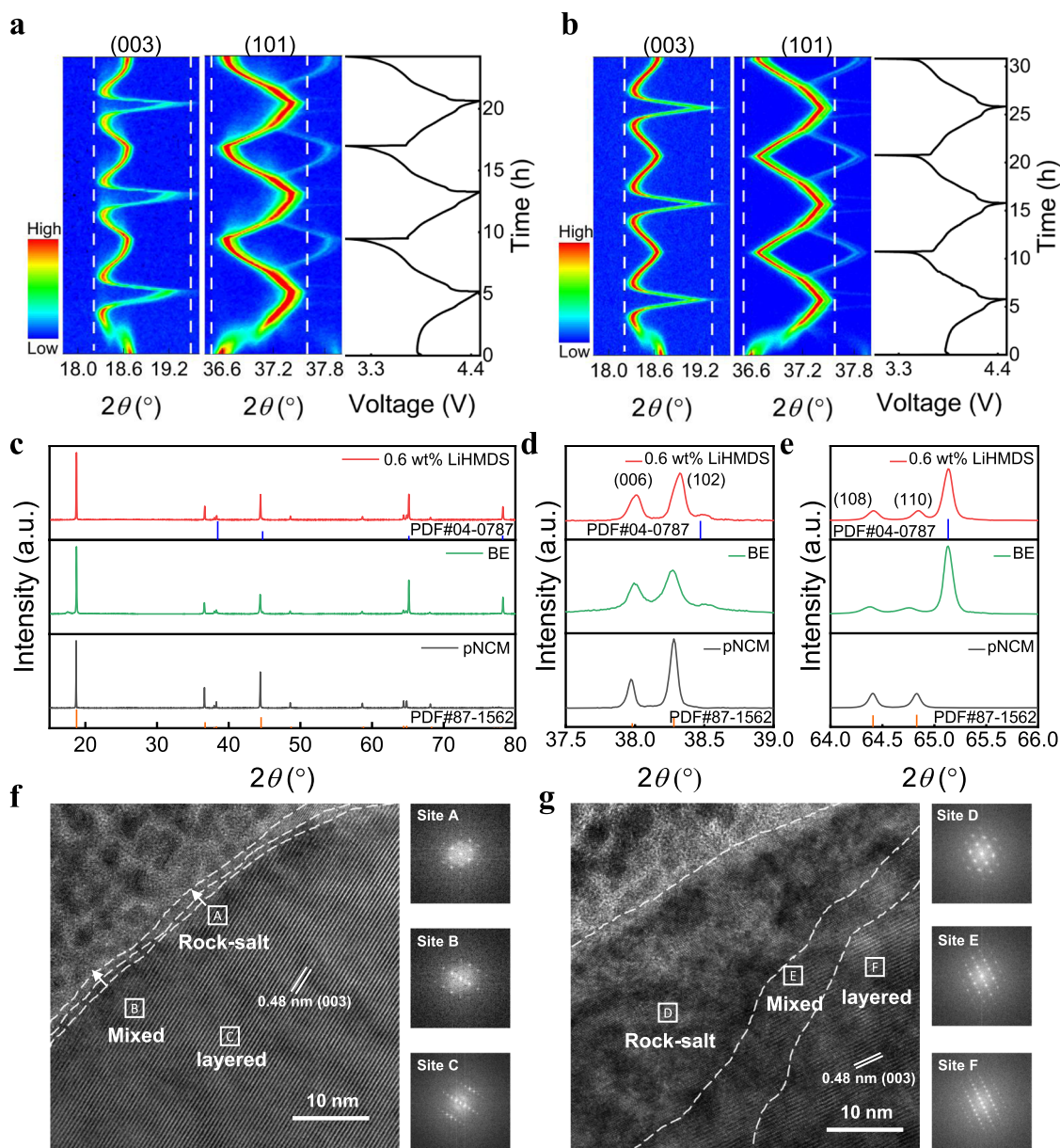


Fig. 3 | Structure characterizations of NCM811 cathode. Operando XRD characterization for NCM811 cathode during the initial three charge-discharge cycles using **a** BE and **b** BE with LiHMDS. The charging/discharging current were 36 mA g^{-1} / 36 mA g^{-1} . **c–e** Ex situ XRD measurements of NCM811 cathode before and after 100 cycles in BE and BE with LiHMDS at 60°C , the charging/discharging current were

180 mA g^{-1} / 180 mA g^{-1} . Ex situ TEM and FFT images of cycled NCM811 cathodes using **f** BE with LiHMDS and **g** BE after 100 cycles at 60°C , the charging/discharging current were 180 mA g^{-1} / 180 mA g^{-1} . The cell was disassembled at fully discharged state.

(Supplementary Fig. 22b). This indicates that the SEI derived from LiHMDS consists of more LiF-like inorganic components, which benefits for the cycling stability of Li metal batteries¹². Moreover, the surface of cycled Li metal electrode using LiHMDS after 100 cycles at 180 mA g^{-1} and 60°C presents a more compact structure than that using BE, indicating the stability of the SEI using LiHMDS. The cross-sectional SEM images show that the thickness of loose structure on cycled Li metal electrode ($\sim 95 \mu\text{m}$) is thicker than that using LiHMDS ($32 \mu\text{m}$) due to the side reactions between Li and BE¹² (Supplementary Fig. 8c, d). This behavior also can be found on the thin Li electrode of $50 \mu\text{m}$ after 10 cycles at 180 mA h g^{-1} (Supplementary Fig. 23).

The content of TM elements in the SEI layer formed in electrolyte with and without LiHMDS is further verified by inductively coupled plasma optical emission spectrometer (ICP-OES) measurement. As shown in Fig. 4a, b, the content of Ni, Co, and Mn in

electrolyte and LMA from Li||NCM811 cell with LiHMDS after 100 cycles at 180 mA g^{-1} under 60°C is much lower than that of Li||NCM811 cell. In particular, the Ni content on the surface of LMA from the Li||NCM811 cell with LiHMDS is $16.83 \mu\text{g mg}^{-1}$, much lower than that from Li||NCM811 cell ($122.53 \mu\text{g mg}^{-1}$). The suppressed TM ions dissolution can be attributed to the formation of a robust CEI on the NCM811 by LiHMDS. In order to further understand the CEI formation process, ex situ nuclear magnetic resonance (NMR) measurements of the cycled electrolyte was used to verify the LiHMDS content after 3 cycles at 36 mA g^{-1} under 60°C . As shown in Supplementary Fig. 24, the HMDS' derivatives signals could be clearly observed before cycling, but it is found that the peaks disappear after 3 cycles 36 mA g^{-1} under 60°C . In addition, we did not find any evidence of $\text{Mn}(\text{HMDS})_2$ or $\text{Ni}(\text{HMDS})_2$. Above results prove that the LiHMDS has been completely consumed after 3

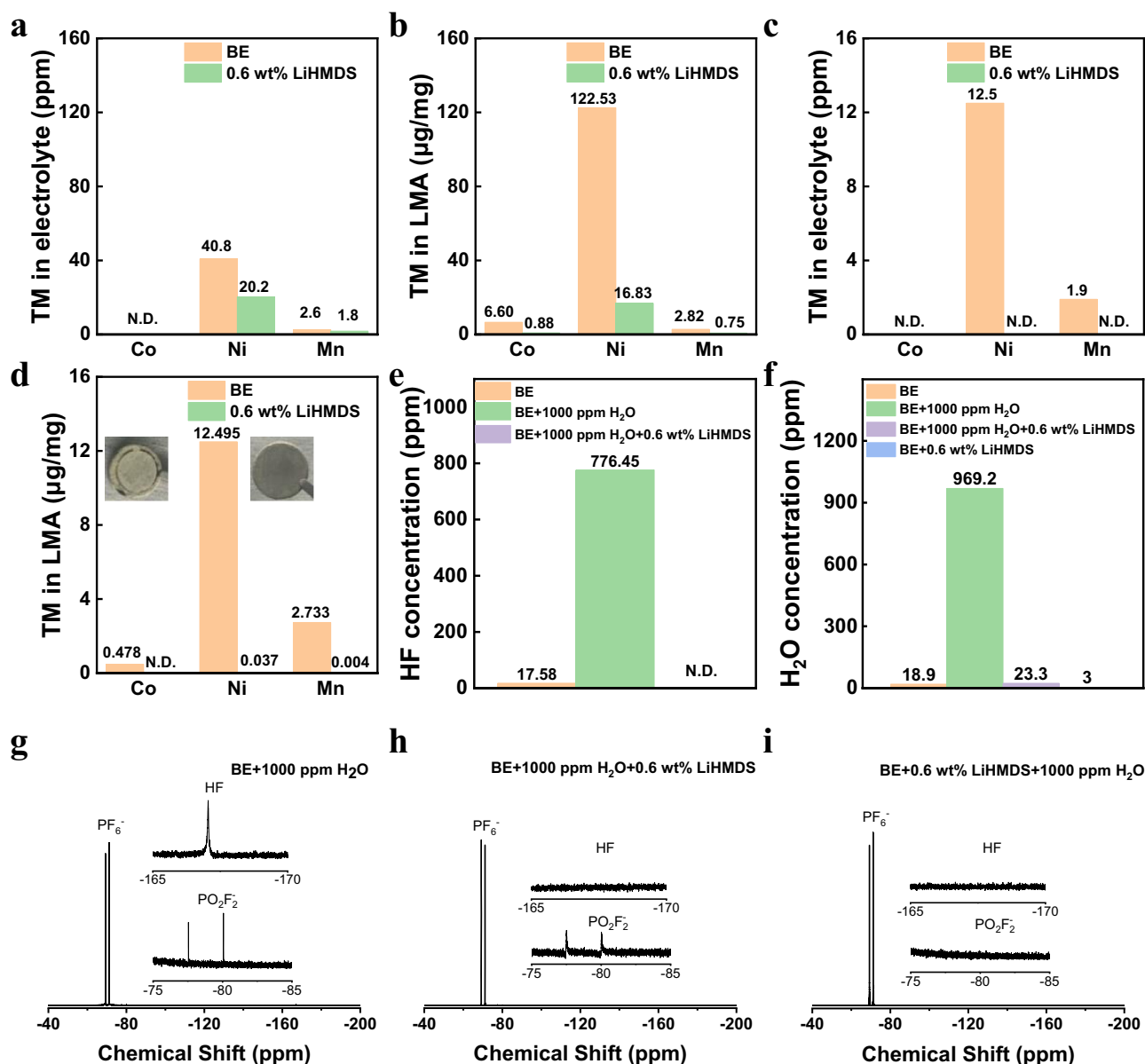


Fig. 4 | Ex situ measurements of the cycled electrolyte solutions and Li metal electrodes. ICP-MS analysis of cycled **a** electrolyte and **b** LMA after 100 cycles at 60 °C, the charging/discharging current were 180 mA g⁻¹/180 mA g⁻¹, the cell was disassembled at fully discharged state. ICP-MS analysis of **c** electrolyte and **d** LMA after rest at open circuit voltage for 7 days at 60 °C. **e** HF concentration of BE,

BE + 1000 ppm H₂O and BE + 0.6 wt% LiHMDS + 1000 ppm H₂O. **f** H₂O concentration of BE, BE + 0.6 wt% LiHMDS, BE + 1000 ppm H₂O and BE + 0.6 wt% LiHMDS + 1000 ppm H₂O. ¹⁹F NMR spectra of the solution of **g** BE + 1000 ppm H₂O, **h** BE + 1000 ppm + 0.6 wt% LiHMDS and **i** BE + 0.6 wt% LiHMDS + 1000 ppm H₂O.

cycles. Since the electrolyte decomposition would be accelerated at elevated temperature, we also measured the TM ions concentration in electrolyte and on the LMA surface after the cells were stored in oven at 60 °C for 7 days. It is found that no TM ions were observed in the electrolyte with LiHMDS and very few TM ions were detected on the LMA surface (Fig. 4c, d), which are much lower than that of the Li||NCM811 cells. Accurate determination of the H₂O and HF content in the electrolyte is essential for understanding the role of LiHMDS. As shown in Fig. 4e, the concentration of HF increases dramatically from 17.58 ppm to 776.45 ppm after adding 1000 ppm H₂O to the BE as measured by acid-base titration method. But after LiHMDS was added to the solution consisting of BE and 1000 ppm H₂O, the solution turns to alkaline, which means that the HF was sequestered by the LiHMDS. Karl Fischer titration method was further adopted to accurately determine the H₂O amount. As shown in Fig. 4f, the H₂O content of

BE is 18.9 ppm, while after LiHMDS was dissolved in the BE and rest for 12 h, the H₂O content sharply decreases to 3 ppm. Even when the H₂O content raises to 969.2 ppm by dropped 5 μL H₂O into 5 mL BE, most of H₂O can be eliminated by LiHMDS. The residual trace H₂O may be caused by moisture in the environment during examination of the H₂O content. To further understand the interaction structures of HF and H₂O with electrolyte, the binding energy and bond length of H₂O-PF₆⁻, HF-HMDS⁻, and H₂O-HMDS⁻ were studied by DFT calculation (Supplementary Fig. 25a, b). It is seen that the HF presents a high binding energy with LiHMDS (Supplementary Fig. 25c), which is almost 2.13 and 10.57 times higher than that of H₂O-HMDS⁻ and H₂O-PF₆⁻. These results support the claim about the LiHMDS capability to eliminate the HF and H₂O in the electrolyte, which is significant and crucial to achieve higher capacity retentions of the Li||NCM811 cells with LiHMDS under harsh conditions.

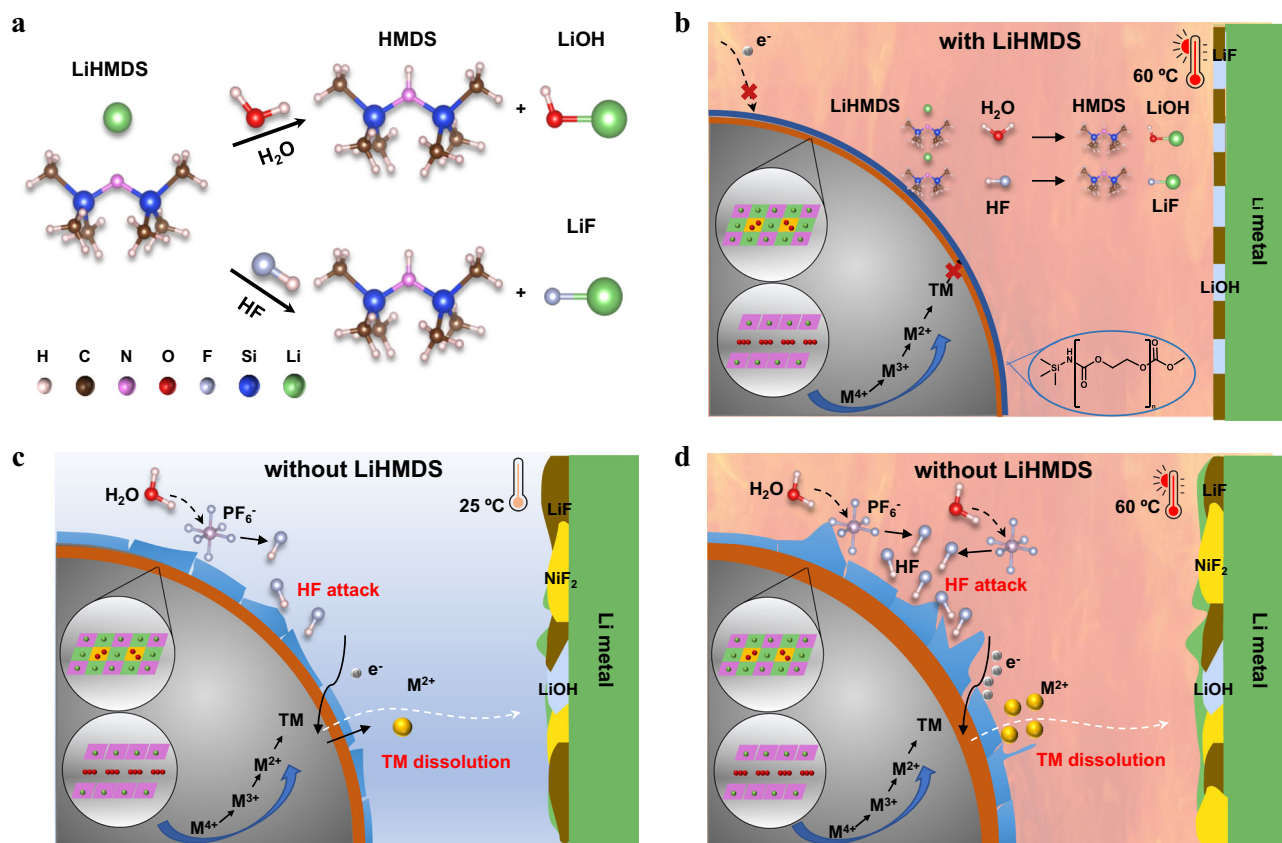


Fig. 5 | Function schematic illustration of LiHMDS in Li||NCM811 cells. a Reaction mechanism of LiHMDS with HF and H₂O. **b–d** Working mechanism of Li||NCM811 cells with/without LiHMDS cells at 25 °C and 60 °C.

Discussion

Mechanisms of LiHMDS for removing HF

To understand the reaction mechanism of LiHMDS with HF and H₂O, the ¹⁹F NMR measurements on various electrolyte solutions were carried out. After adding 1000 ppm H₂O into the BE and stored at 25 °C for 1 day, the ¹⁹F NMR spectra shows two doublet peaks and one singlet peak (Fig. 4g). The doublet peak located at -71.2 ppm and -79.3 ppm is associated with the PF₆⁻ in LiPF₆. The other doublet peak (-77.5 and -80.1 ppm) and the singlet peak (-167.1 ppm) are corresponding to the PO₂F₂ and HF, respectively⁴⁵. Moreover, we added 1000 ppm H₂O into BE with LiHMDS and carried out the ¹⁹F NMR measurements. Intriguingly, after adding LiHMDS into BE with 1000 ppm H₂O, the peak of HF was not detectable (Fig. 4h) and only one doublet peak of PF₆⁻ can be observed (Fig. 4i). Above results demonstrate that the LiHMDS reacts with H₂O more actively than the LiPF₆ and can eliminate HF in the electrolyte. The thermal stability of BE and electrolyte with LiHMDS in Li||NCM811 cells at high temperature was also evaluated by ¹⁹F NMR measurements. The Li||NCM811 cells were assembled and stored at 60 °C for 7 days without cycling and disassembled in an Ar-filled glovebox before testing. As shown in Supplementary Fig. 26a, the peak of HF was not detected in BE, which might be ascribed to the reactions of HF with LMA and NCM811 particles. However, the byproduct of PO₂F₂ derived from the thermal decomposition of LiPF₆ could be clearly observed, while which cannot be found in the electrolyte with LiHMDS (Supplementary Fig. 26b), further demonstrating that the LiHMDS could significantly improve the thermal stability of electrolyte. We also examined the cycling performance of the Li||NCM811 cells with 1000 ppm H₂O in the electrolytes at 180 mA g⁻¹ under 60 °C (Supplementary Fig. 27a). The coulombic efficiency of the full cells cycled using BE with 1000 ppm H₂O is only 37.41% at the first cycle and the charge curve is abnormal (Supplementary Fig. 27b), suggesting the severe side

reactions between LiPF₆ and H₂O during charging. In sharp contrast, the Li||NCM811 cells with LiHMDS and 1000 ppm H₂O presents a higher initial coulombic efficiency (68.37%) and delivers a discharge capacity of 217.9 mA h g⁻¹.

From the experimental and theoretical results, the function of LiHMDS is illustrated schematically in Fig. 5. Owing to the high binding energy of HMDS⁻ with H₂O and HF and the intrinsic organic base nature of LiHMDS, the LiHMDS could capture H₂O and HF quickly (Fig. 5a). Therefore, in the Li||NCM811 cells with LiHMDS at 60 °C, the LiHMDS not only captures HF and H₂O in the electrolyte, but also constructs uniform, thin and robust CEI layer before oxidation of electrolyte, which inhibits the TM ions dissolution and improves the cyclic performance at high voltage and temperature (Fig. 5b). However, in the Li||NCM811 cells at 25 °C, trace amount of water reacts with the LiPF₆ to generate HF, which damages the CEI derived from oxidation of electrolyte that leads to the TM ions dissolution and causes the capacity fade of NCM811 and cation ion mixing (Fig. 5c). At 60 °C, the side reactions such as LiPF₆ decomposition, TM dissolution and their shuttle effect in the Li||NCM811 cells are more serious than those in 25 °C, which leads to worse cell performance (Fig. 5d).

In summary, we investigated a non-aqueous electrolyte additive of LiHMDS with low oxidation potential for long cycling Li||NCM811 batteries at both high voltage of 4.5 V and high temperature of 60 °C. The Li||NCM811 batteries with 0.6% LiHMDS cycled between 3.0 and 4.5 V demonstrates a capacity retention of 73.92% after 1000 cycles at 25 °C and 66.02% after 500 cycles at 60 °C and 180 mA g⁻¹. The LiHMDS not only efficiently depletes HF and H₂O (even 1000 ppm) in the electrolyte, but also is preferentially oxidized prior to electrolyte to construct a thin, uniform and robust CEI on NCM811 cathode surface, which can suppress the side reactions with electrolyte, phase transformation of NCM811 from layered structure to rock-salt phase and

endows NCM811 cathode with good thermal shock resistance. As a result, the TM ions dissolution of NCM811 and their attack for SEI on the LMA are successfully suppressed, which improves the cycling stability of Li||NCM811 batteries at both high voltage and high temperature.

Methods

Materials

The commercial $\text{LiNi}_{0.8}\text{Co}_{0.1}\text{Mn}_{0.1}\text{O}_2$ (NCM811, $D_{50} = 3.77 \mu\text{m}$), $\text{LiNi}_{0.5}\text{Mn}_{1.5}\text{O}_2$ (LNMO, $D_{50} = 11.61 \mu\text{m}$), polyvinylidene difluoride (PVDF5130, $M_w = 1,200,000 \text{ Da}$, particle size: $100 \mu\text{m}$, 99.5%), Super P (particle size: $40\text{--}50 \text{ nm}$, 99.5%), lithium polyacrylate (PAALi, 4 wt% in water), Graphite ($D_{50} = 19.2 \mu\text{m}$, 99.5%), Al foil (thickness: $10 \mu\text{m}$, 99.9%), Cu foil (thickness: $10 \mu\text{m}$, 99.9%), separator (Celgard 2500, thickness: $25 \mu\text{m}$, monolayer PP membrane, pore size: average diameter $0.064 \mu\text{m}$, porosity: $55 \pm 5\%$), Coin cell components (CR2032, spacer: $15.8 \times 1 \text{ mm}$, spring: $15.4 \times 1.1 \text{ mm}$) and the baseline electrolyte (BE) (1 M LiPF_6 in EC, EMC and DMC (1:1:1 by volume), ($\text{H}_2\text{O} < 20 \text{ ppm}$)) were purchased from Guangdong Canrd New Energy Technology Co., Ltd. Lithium hexamethyldisilazide (LiHMDS, 97%) came from Sigma-Aldrich. N-methyl-2-pyrrolidone (NMP, AR) and DMC (99%, ($\text{H}_2\text{O} < 20 \text{ ppm}$)) were purchased from Shanghai Aladdin Biochemical Technology Co., Ltd. Lithium foil (thickness: $450 \mu\text{m}$, diameter: $15.6 \mu\text{m}$) and double side coated Cu foil ($20 \mu\text{m}$ Li each side and the thickness of Cu is $10 \mu\text{m}$, the whole thickness of Li anode is $50 \mu\text{m}$) came from China Energy Lithium Co., Ltd. Dimethyl sulfoxide-d6 (DMSO-d6, 0.6 mL, 99.9%, +0.03% V/V tetramethyl silane (TMS)) came from Shanghai Macklin Biochemical Technology Co., Ltd. All materials were used as received. To prepare electrolytes with 0.6 wt% LiHMDS, 16.7 mg LiHMDS was dissolved in 2 mL BE by magnetic stirring at $25 \pm 2 \text{ }^\circ\text{C}$ for 30 min.

Fabrication of cells

NCM811 and LNMO cathode was prepared by following steps. The mixture of 0.8 g (80 wt%) single crystal NCM811 (or LNMO) powder, 0.1 g (10 wt%) PVDF5130 and 0.1 g (10 wt%) Super P was manually grinded in an agate mortar for 10 min in an air environment and then dispersed in 2 mL NMP by magnetic stirring for 4 h to form a slurry. Then the slurry was casted on an Al foil and dried at $120 \text{ }^\circ\text{C}$ for 2 h under vacuum. Graphite anode was prepared by following steps. 1 g (4 wt%) PAALi was diluted by 1 mL H_2O , then 0.15 g (1.5 wt%) Super P was added to the solution and stirring for 30 mins, and added 0.945 g (94.5 wt%) graphite in the emulsion and stirring for 4 h to form a slurry. Then the slurry was casted on a Cu foil and dried at $80 \text{ }^\circ\text{C}$ for 8 h under vacuum. The CR2032 Li||NCM811, Graphite||NCM811 and Li||LNMO coin cells were assembled in an Ar-filled glove box (O_2 and $\text{H}_2\text{O} < 0.1 \text{ ppm}$) using $50 \mu\text{L}$ BE with/without LiHMDS. The thickness of lithium foil is $450 \mu\text{m}$ and the diameter is 15.6 mm . The diameter of cathode is 12 mm , and the thickness of separator is $25 \mu\text{m}$. In the coin cell, 2 spacers and a spring was used in the cell. The separator was Celgard2500. For Li||NCM811 pouch cell, two single side coated cathode (mass loading: $\sim 10 \text{ mg cm}^{-2}$, $4 \text{ cm} \times 3.5 \text{ cm}$) and one double coated anode ($4.3 \text{ cm} \times 4 \text{ cm}$) were stacked one by one and separated by Celgard 2500 ($4.5 \text{ cm} \times 4.5 \text{ cm}$), the electrolyte volume is $200 \mu\text{L}$. We assembled in a dry room whose dew point is $\sim 50 \text{ }^\circ\text{C}$.

Electrochemical measurements

The LSV measurements of Li||stainless steel coin cells with different electrolytes were examined from 2.5 to 5.5 V vs. Li at a scanning rate of 0.5 mV s^{-1} under $60 \text{ }^\circ\text{C}$ using a VMP3 multichannel electrochemical station (Bio Logic Science Instruments, France). The cyclic voltammetry (CV) measurements of Li||NCM811 cells were examined between 3 and 4.5 V at a scanning rate of 0.05 mV s^{-1} under $25 \text{ }^\circ\text{C}$ and $60 \text{ }^\circ\text{C}$ using a VMP3. The electrochemical impedance spectroscopy (EIS) of Li||NCM811 cells was performed from 7 MHz to 10 mHz at an amplitude of 5 mV, 6 data points per decade, and the 3.95 V of charging progress

(after charge to 3.95 V, a constant-voltage charging was applied until the specific current is lower than 9 mA g^{-1} , and rest for 2 h) applied before carrying out the EIS measurements at $60 \text{ }^\circ\text{C}$ using a VMP3. Cycling and rate performances of Li||NCM811 cells were measured at $25 \text{ }^\circ\text{C}$ and $60 \text{ }^\circ\text{C}$ on a battery test system (LAND CT-2001A) with a voltage range from 3 to 4.5 V. The electrochemical floating test was performed in Li||NCM811 cells with different electrolyte. The cells were first charged to 4.5 V at 18 mA g^{-1} and then maintained for 12 h with the current monitored by LAND battery test system. For all electrochemical measurement, four cells were measured at the same condition. And the specific current and specific capacity refers to the mass of the active material in the cathode. The electrochemical energy storage tests at various temperatures were carried out in a constant temperature chamber.

Materials characterization

The X-ray diffraction (XRD) measurements of the samples were carried out on a Rigaku Smartlab with $\text{Cu-K}\alpha$ radiation. The operando XRD test during charging and discharging rate of 36 mA g^{-1} were performed at $60 \text{ }^\circ\text{C}$ and diffraction patterns were collected every 8 min. The morphologies and structures of NCM cathode and Li anode were characterized by a scanning electron microscope (SEM, HITACH S4800) with energy dispersive spectroscopy (EDS) and a field emission transmission electron microscope (FE-TEM, FEI Tecnai F30). X-ray photoelectron spectroscopy (XPS) measurements was collected on a PHI 5000 VersaProbe II instrument. The ^{19}F and ^1H nuclear magnetic resonance (NMR) data were collected with NMR spectrometer (ADVANCED III 400 MHz, Bruker, Switzerland) with DMSO-*d*6 solvent. The type of NMR-Tube is WILMAD WF-1000-7 5 mm. To prepare the samples for NMR, we assembled the Li||NCM811 coin cells with/without LiHMDS, which were stored at $60 \text{ }^\circ\text{C}$ for 7 days. Then we disassembled the cells and washed the separator with 0.6 mL DMSO-*d*6 and collected the solution for NMR measurement in the Ar-filled glovebox. The transition metal (TM) concentration of electrolyte and TM content of Li anode was measured by inductively coupled plasma optical emission spectrometer (ICP-OES, SpectroArcos II MV, Germany). The cycled LMA was dissolved in 10 mL 1 M HCl, and the TM content on the surface of LMA is calculated by the mass of TM elements in the solution over the mass of active material in the NCM811 cathode. For the TM concentration of electrolyte, we soaked the cathode, separator and anode in 5 mL DMC for 5 min and collected all the liquid in the Ar-filled glovebox, then the solvent was evaporated in oven under $80 \text{ }^\circ\text{C}$, and the residues was dissolved in 1 mL 1 M HCl and then dilute to 10 mL solution with 9 mL deionized H_2O using 10 mL volumetric flask. For the TM content of LMA surface, the washed LMA was dissolved in 2 mL 1 M HCl and then dilute to 10 mL solution with deionized H_2O using 10 mL volumetric flask. The CEI component data was collected by time-of-flight secondary ion mass spectrometry (ToF-SIMS, PHI nanoTOF II, 30 keV, 2 nA, and the raster size is $60 \times 60 \mu\text{m}$). The cross-sectional NCM cathode is investigated by ion milling system (IMS, HITACH IM4000 plus). For HF content test, BE + 1000 ppm H_2O + 0.6 wt% LiHMDS means that we added 1000 ppm to BE and the obtained solution was stored for 4 h, and then 0.6 wt% LiHMDS was added afterward and stored for 4 h again. The purpose of this experiment is to confirm the role of LiHMDS for eliminating HF. BE + 0.6 wt% LiHMDS + 1000 ppm H_2O means that after 0.6 wt% LiHMDS was dissolved in BE, 1000 ppm H_2O was added to the solution and the LiHMDS can absorb the H_2O . The HF and H_2O content of electrolyte was measured by acid-base titration method and Karl Fischer titration method, and sample preparation of electrolyte is the same as ^{19}F NMR measurement. Prior to analysis, the cells were disassembled in Ar-filled glove box (Mikrouna) ($\text{H}_2\text{O} < 0.1 \text{ ppm}$, $\text{O}_2 < 0.1 \text{ ppm}$) and the electrode surfaces were rinsed with 5 mL of DMC. After drying at $25 \text{ }^\circ\text{C}$ in glovebox for 10 min, the electrodes were transferred by the transfer sample holder with an Ar-filled to isolate the air.

Computational methods

The highest occupied molecular orbital and lowest unoccupied molecular orbital (HOMO and LUMO) energy of EC, EMC, DMC, LiPF₆ and LiHMDS was calculated by quantum-chemical calculations (based on density functional theory, B3LYP/6-311G (d, p)). The optimum structures were optimized by B3LYP method in combination with the 6-31G (d, p) basis set and the more precise energy was calculated by same method in combination with the 6-311G++ (d, p) basis set. The vibration frequency and intrinsic reaction coordinate (IRC) analysis were adopted to confirm each transition state (TS) that connects both product and reactant in the same pathway at the same level. The stable structure between H₂O and Li⁺, PF₆⁻ and HDMS⁻ were obtained from the Molecular dynamics (MD) simulation with the force-fields of water model involving four charge sites (TIP4P)⁴⁶ and the optimized potentials for liquid simulations (OPLS-AA)⁴⁷ and assigned with RESP charges⁴⁸.

Reporting summary

Further information on research design is available in the Nature Portfolio Reporting Summary linked to this article.

Data availability

The authors declare that all the relevant data are available within the paper and its Supplementary Information file or from the corresponding author upon reasonable request.

References

1. Manthiram, A., Song, B. & Li, W. A perspective on nickel-rich layered oxide cathodes for lithium-ion batteries. *Energy Stor. Mater.* **6**, 125–139 (2016).
2. Li, W., Erickson, E. M. & Manthiram, A. High-nickel layered oxide cathodes for lithium-based automotive batteries. *Nat. Energy* **5**, 26–34 (2020).
3. Liu, J. et al. Pathways for practical high-energy long-cycling lithium metal batteries. *Nat. Energy* **4**, 180–186 (2019).
4. Schmich, R., Wagner, R., Hörpel, G., Placke, T. & Winter, M. Performance and cost of materials for lithium-based rechargeable automotive batteries. *Nat. Energy* **3**, 267–278 (2018).
5. Liu, L. et al. Layered ternary metal oxides: performance degradation mechanisms as cathodes, and design strategies for high-performance batteries. *Prog. Mater. Sci.* **111**, 100655 (2020).
6. Ren, X. et al. Enabling high-voltage lithium-metal batteries under practical conditions. *Joule* **3**, 1662–1676 (2019).
7. Goodenough, J. B. & Park, K.-S. The Li-ion rechargeable battery: a perspective. *J. Am. Chem. Soc.* **135**, 1167–1176 (2013).
8. Yang, H. et al. Simultaneously dual modification of Ni-rich layered oxide cathode for high-energy lithium-ion batteries. *Adv. Funct. Mater.* **29**, 1808825 (2019).
9. Lin, F. et al. Surface reconstruction and chemical evolution of stoichiometric layered cathode materials for lithium-ion batteries. *Nat. Commun.* **5**, 3529 (2014).
10. Lin, F. et al. Profiling the nanoscale gradient in stoichiometric layered cathode particles for lithium-ion batteries. *Energy Environ. Sci.* **7**, 3077–3085 (2014).
11. Lin, F. et al. Metal segregation in hierarchically structured cathode materials for high-energy lithium batteries. *Nat. Energy* **1**, 15004 (2016).
12. Xue, W. et al. Ultra-high-voltage Ni-rich layered cathodes in practical Li metal batteries enabled by a sulfonamide-based electrolyte. *Nat. Energy* **6**, 495–505 (2021).
13. Liu, W. et al. Nickel-rich layered lithium transition-metal oxide for high-energy lithium-ion batteries. *Angew. Chem. Int. Ed.* **54**, 4440–4457 (2015).
14. Liu, M. et al. Hydrolysis of LiPF₆-containing electrolyte at high voltage. *ACS Energy Lett.* **6**, 2096–2102 (2021).
15. Chang, Z. et al. A stable high-voltage lithium-ion battery realized by an in-built water scavenger. *Energy Environ. Sci.* **13**, 1197–1204 (2020).
16. Han, J.-G., Kim, K., Lee, Y. & Choi, N.-S. Scavenging materials to stabilize LiPF₆-containing carbonate-based electrolytes for Li-ion batteries. *Adv. Mater.* **31**, 1804822 (2019).
17. Kim, K. et al. Cyclic aminosilane-based additive ensuring stable electrode–electrolyte interfaces in Li-ion batteries. *Adv. Energy Mater.* **10**, 2000012 (2020).
18. Kim, K., Ma, H., Park, S. & Choi, N.-S. Electrolyte-additive-driven interfacial engineering for high-capacity electrodes in lithium-ion batteries: promise and challenges. *ACS Energy Lett.* **5**, 1537–1553 (2020).
19. Lebens-Higgins, Z. W. et al. Evolution of the electrode–electrolyte interface of LiNi_{0.8}Co_{0.15}Al_{0.05}O₂ electrodes due to electrochemical and thermal stress. *Chem. Mater.* **30**, 958–969 (2018).
20. Wang, D. et al. Role of zirconium dopant on the structure and high voltage electrochemical performances of LiNi_{0.5}Co_{0.2}Mn_{0.3}O₂ cathode materials for lithium ion batteries. *Electrochim. Acta* **188**, 48–56 (2016).
21. Liu, S. et al. Uncovering the role of Nb modification in improving the structure stability and electrochemical performance of LiNi_{0.6}Co_{0.2}Mn_{0.2}O₂ cathode charged at higher voltage of 4.5 V. *J. Power Sources* **374**, 149–157 (2018).
22. Neudeck, S. et al. Room temperature, liquid-phase Al₂O₃ surface coating approach for Ni-rich layered oxide cathode material. *Chem. Commun.* **55**, 2174–2177 (2019).
23. Han, B. et al. Enhancing the structural stability of Ni-rich layered oxide cathodes with a preformed Zr-concentrated defective nanolayer. *ACS Appl. Mater. Interfaces* **10**, 39599–39607 (2018).
24. Schipper, F. et al. From surface ZrO₂ coating to bulk Zr doping by high temperature annealing of nickel-rich lithiated oxides and their enhanced electrochemical performance in lithium ion batteries. *Adv. Energy Mater.* **8**, 1701682 (2018).
25. He, H., Zan, L. & Zhang, Y. Effects of amorphous V₂O₅ coating on the electrochemical properties of Li[Li_{0.2}Mn_{0.54}Ni_{0.13}Co_{0.13}]O₂ as cathode material for Li-ion batteries. *J. Alloy. Compd.* **680**, 95–104 (2016).
26. Kim, K., Ma, H., Park, S. & Choi, N.-S. Electrolyte-additive-driven interfacial engineering for high-capacity electrodes in lithium-ion batteries: Promise and challenges. *ACS Energy Lett.* **5**, 1537–1553 (2020).
27. Zhang, S. S. Aromatic isocyanate as a new type of electrolyte additive for the improved performance of Li-ion batteries. *J. Power Sources* **163**, 567–572 (2006).
28. Jang, S. H. & Yim, T. Effect of silyl ether-functionalized dimethoxydimethylsilane on electrochemical performance of a Ni-rich NCM cathode. *ChemPhysChem* **18**, 3402–3406 (2017).
29. Yang, J. et al. Electrolytes polymerization-induced cathode–electrolyte-interphase for high voltage lithium-ion batteries. *Adv. Energy Mater.* 2101956 (2021).
30. Kim, H. et al. Enhancing interfacial bonding between anisotropically oriented grains using a glue-nanofiller for advanced Li-Ion battery cathode. *Adv. Mater.* **28**, 4705–4712 (2016).
31. Verma, P., Maire, P. & Novák, P. A review of the features and analyses of the solid electrolyte interphase in Li-ion batteries. *Electrochim. Acta* **55**, 6332–6341 (2010).
32. Selman, J. R., Al Hallaj, S., Uchida, I. & Hirano, Y. Cooperative research on safety fundamentals of lithium batteries. *J. Power Sources* **97–98**, 726–732 (2001).
33. Holoubek, J. et al. An all-fluorinated ester electrolyte for stable high-voltage Li metal batteries capable of ultra-low-temperature operation. *ACS Energy Lett.* **5**, 1438–1447 (2020).
34. Zheng, X. et al. High-voltage performance of LiNi_{1/3}Co_{1/3}Mn_{1/3}O₂/graphite batteries with di(methylsulfonyl) methane as a new

- sulfone-based electrolyte additive. *J. Power Sources* **293**, 196–202 (2015).
35. Klein, S. et al. Understanding the outstanding high-voltage performance of NCM523||graphite lithium ion cells after elimination of ethylene carbonate solvent from conventional electrolyte. *Adv. Energy Mater.* **11**, 2003738 (2021).
 36. Noh, H.-J., Youn, S., Yoon, C. S. & Sun, Y.-K. Comparison of the structural and electrochemical properties of layered $\text{Li}[\text{Ni}_x\text{Co}_y\text{Mn}_z]\text{O}_2$ ($x = 1/3, 0.5, 0.6, 0.7, 0.8$ and 0.85) cathode material for lithium-ion batteries. *J. Power Sources* **233**, 121–130 (2013).
 37. Yim, T. et al. Effect of acid scavengers on electrochemical performance of lithium–sulfur batteries: functional additives for utilization of LiPF_6 . *Jpn. J. Appl. Phys.* **53**, 08NK01 (2014).
 38. Jiao, S. et al. Stable cycling of high-voltage lithium metal batteries in ether electrolytes. *Nat. Energy* **3**, 739–746 (2018).
 39. Zheng, Y. et al. Construction of a stable $\text{LiNi}_{0.8}\text{Co}_{0.1}\text{Mn}_{0.1}\text{O}_2$ (NCM811) cathode interface by a multifunctional organosilicon electrolyte additive. *ACS Appl. Energy Mater.* **3**, 2837–2845 (2020).
 40. Liu, T. et al. Understanding Co roles towards developing Co-free Ni-rich cathodes for rechargeable batteries. *Nat. Energy* **6**, 277–286 (2021).
 41. Wei, Y. et al. Kinetics tuning of Li-ion diffusion in layered $\text{Li}(\text{Ni}_x\text{Mn}_y\text{Co}_z)\text{O}_2$. *J. Am. Chem. Soc.* **137**, 8364–8367 (2015).
 42. Li, Z. et al. Stabilizing the interphasial layer of Ni-rich cathode and graphite anode for lithium ion battery with multifunctional additive. *J. Power Sources* **467**, 228343 (2020).
 43. Yan, P. et al. Intragranular cracking as a critical barrier for high-voltage usage of layer-structured cathode for lithium-ion batteries. *Nat. Commun.* **8**, 14101 (2017).
 44. Li, W., Kim, U.-H., Dolocan, A., Sun, Y.-K. & Manthiram, A. Formation and inhibition of metallic lithium microstructures in lithium batteries driven by chemical crossover. *ACS Nano* **11**, 5853–5863 (2017).
 45. Yang, X. et al. Mechanism of cycling degradation and strategy to stabilize a nickel-rich cathode. *J. Mater. Chem. A* **6**, 16149–16163 (2018).
 46. Jorgensen, W. L., Chandrasekhar, J., Madura, J. D., Impey, R. W. & Klein, M. L. Comparison of simple potential functions for simulating liquid water. *J. Chem. Phys.* **79**, 926–935 (1983).
 47. Robertson, M. J., Tirado-Rives, J. & Jorgensen, W. L. Improved Peptide and Protein Torsional Energetics with the OPLSAA Force Field. *J. Chem. Theory Comput.* **11**, 3499–3509 (2015).
 48. Bayly, C. I., Cieplak, P., Cornell, W. & Kollman, P. A. A well-behaved electrostatic potential based method using charge restraints for deriving atomic charges: the RESP model. *J. Phys. Chem.* **97**, 10269–10280 (2002).

Acknowledgements

This work was supported by the National Key Research and Development Program of China (2021YFF0500600), National Natural Science Foundation of China (No. U2001220), Local Innovative Research Teams

Project of Guangdong Pearl River Talents Program (No. 2017BT01N111), Shenzhen All-Solid-State Lithium Battery Electrolyte Engineering Research Center (XMHT20200203006), and Shenzhen Technical Plan Project (Nos. RCJC20200714114436091, JCYJ20180508152210821, and JCYJ20180508152135822).

Author contributions

D.F.Z. and M.L. contributed equally to this work. Y.-B.H. conceived and supervised the project. D.F.Z., M.L., and Y.-B.H. designed the experiments. D.F.Z. performed the experiments with the help from M.L., C.Z., P.W., Y.B.H., and Z.C. J.B.M. completed the computational work. Y.P.W. conducted the TEM test. D.F.Z. and M.Z. assumed the reaction mechanism of LiHMDS additives. Y.-B.H., D.F.Z., M.L., K.K.L., W.L., Q.-H.Y., and F.Y.K. discussed the results. D.F.Z., M.L., K.Y., K.K.L., Y.-B.H., and F.Y.K. wrote the initial manuscript which was approved by all the authors.

Competing interests

The authors declare no competing interests.

Additional information

Supplementary information The online version contains supplementary material available at <https://doi.org/10.1038/s41467-022-34717-4>.

Correspondence and requests for materials should be addressed to Yan-Bing He.

Peer review information *Nature Communications* thanks the anonymous reviewer(s) for their contribution to the peer review of this work.

Reprints and permissions information is available at <http://www.nature.com/reprints>

Publisher's note Springer Nature remains neutral with regard to jurisdictional claims in published maps and institutional affiliations.

Open Access This article is licensed under a Creative Commons Attribution 4.0 International License, which permits use, sharing, adaptation, distribution and reproduction in any medium or format, as long as you give appropriate credit to the original author(s) and the source, provide a link to the Creative Commons license, and indicate if changes were made. The images or other third party material in this article are included in the article's Creative Commons license, unless indicated otherwise in a credit line to the material. If material is not included in the article's Creative Commons license and your intended use is not permitted by statutory regulation or exceeds the permitted use, you will need to obtain permission directly from the copyright holder. To view a copy of this license, visit <http://creativecommons.org/licenses/by/4.0/>.

© The Author(s) 2022